PCCP

RSC Publishing

PAPER

View Article Online
View Journal | View Issue

Cite this: *Phys. Chem. Chem. Phys.*, 2013, **15**, 20698

Electrospun sillenite $Bi_{12}MO_{20}$ (M = Ti, Ge, Si) nanofibers: general synthesis, band structure, and photocatalytic activity†

Dongfang Hou,[ab] Xianluo Hu,*[a] Yanwei Wen,[a] Bin Shan,*[a] Pei Hu,[a] Xiaoqin Xiong,[a] Yun Qiao[a] and Yunhui Huang[a]

Received 18th September 2013,
Accepted 21st October 2013

DOI: 10.1039/c3cp53945h

www.rsc.org/pccp

Sillenite $Bi_{12}MO_{20}$ (M = Ti, Ge, Si) nanofibers have been fabricated through a facile electrospinning route for photocatalytic applications. Uniform $Bi_{12}MO_{20}$ (M = Ti, Ge, Si) nanofibers with diameters of 100–200 nm and lengths of up to several millimeters can be readily obtained by thermally treating the electrospun precursors. The photocatalytic activities of these nanofibers for degradation of rhodamine B (RhB) were explored under UV-visible light. The band structure and the degradation mechanisms were also discussed. The fibrous photocatalysts of $Bi_{12}TiO_{20}$, $Bi_{12}SiO_{20}$ and $Bi_{12}GeO_{20}$ exhibit different photocatalytic behaviours, which are attributed to the microstructure, band gap, and electronic structures.

Introduction

Efficient photocatalytic processes unveil important opportunities to tackle the global energy demand and environmental pollution problems.[1–3] Highly effective and environmentally friendly photocatalysts of metal oxides have been developed to convert solar energy into chemical energy.[4,5] Among them, a variety of semiconductor-type metal oxides have been so far investigated as photocatalysts for environmental purification and energy conversion.[6–9] They are usually divided into three groups in terms of the electronic configuration of their core metal ions: transition metal ions with d^0 configuration, rare-earth metal ions with f^0 configuration, and typical metal ions with d^{10} configuration. The core metal ion is suggested to be one of the most critical factors to design new photocatalysts.[10]

Since the transition-metal ion of Bi^{3+} possesses the same electronic configuration as Ga^{3+} and Sn^{4+} in several typical photocatalysts, it should be the viable core metal ion for photocatalysts.[11] Bi-based oxides such as Bi_2WO_6,[5] BiOI,[9] Bi_2O_3,[12] BiOCl,[13] $BiVO_4$,[14] Bi_2MoO_6,[15] $Bi_4Ti_3O_{12}$,[16] and $CaBi_2O_4$ (ref. 17) have been widely investigated as photocatalysts because of their unique crystal structures and high activities. $Bi_{12}MO_{20}$ (BMO, M = Ti, Ge, and Si) oxides belong to a family of sillenite compounds with a body-centered cubic crystal structure (space group *I*23). $Bi_{12}TiO_{20}$ (BTO), $Bi_{12}SiO_{20}$ (BSO), and $Bi_{12}GeO_{20}$ (BGO) are isostructural and have quasi-identical chemical compositions.[18] MO_4 tetrahedra exist both on the corners and at the cube center in the BMO structure. Each bismuth atom is surrounded by seven oxygen atoms, which may be considered as a distorted octahedral.[19] The BMOs are of great importance because of their interesting photorefractive, photochromic, dielectric properties[20–22] and promising industrial applications in the fields of optical signal processing, phase conjugation, image amplification, holographic data storage, real-time holography, and optical communications.[22,23] In recent years, the photocatalytic properties of BMOs have also attracted increasing attention for decomposing organic pollutants. For instance, Yao *et al.*[24] reported that $Bi_{12}TiO_{20}$ with a band gap of about 2.4 eV and Ba-doped $Bi_{12}TiO_{20}$ (ref. 25) exhibited a high photocatalytic activity to photodegrade methyl orange under UV irradiation. The spherical $Bi_{12}TiO_{20}$ (ref. 26) with a band gap of about 2.65 eV was synthesized by a hydrothermal method and exhibited enhanced photocatalytic activity in the photodegradation of acid orange 7 under visible-light irradiation.[27] Complex $Bi_{12}TiO_{20}$ architectures with a band gap of about 2.55 eV were prepared for the degradation of RhB under visible-light irradiation.[19] Besides $Bi_{12}TiO_{20}$, the photocatalytic properties of $Bi_{12}SiO_{20}$ and $Bi_{12}GeO_{20}$ have also received much attention.[28,29]

One-dimensional (1D) nanostructured inorganic semiconductors, such as nanowires, nanotubes and nanofibers, have aroused much attention in recent years as potential building blocks for nanoscale electronics, optoelectronics, optical sensing, and energy harvesting.[30] Superior performances have been demonstrated, arising from their

[a] *State Key Laboratory of Materials Processing and Die & Mould Technology, School of Materials Science and Engineering, Huazhong University of Science and Technology, Wuhan 430074, China. E-mail: huxl@mail.hust.edu.cn, bshan@mail.hust.edu.cn*

[b] *College of Mechanical and Material Engineering, Three Gorges University, Yichang 443002, China*

† Electronic supplementary information (ESI) available. See DOI: 10.1039/c3cp53945h

relatively high carrier mobility, high surface areas and size-related intriguing physical properties.[30,31] Electrospinning is a most convenient, economical and direct technique that allows the fabrication of 1D continuous fibers with diameters down to a few nanometers. Significant efforts have been devoted to developing 1D electrospun semiconductor photocatalysts with high surface areas, porosities, and remarkable transport characteristics of electrons and holes, and thus leading to enhanced photocatalytic activities.[32] In our previous work,[16] porous $Bi_4Ti_3O_{12}$ nanofibers with diameters of 50–100 nm have been fabricated by electrospinning and exhibit enhanced visible-light-driven photocatalytic activity. In addition, electrospinning combined with other strategies including doping,[33] hydrothermal techniques,[31] and successive ionic layer adsorption and reaction (SILAR)[34] is developed to prepare other well-defined 1D nanostructures. It is an exciting and promising direction for developing novel multifunctional and advanced materials.

Here we report a general facile electrospinning method to synthesize $Bi_{12}MO_{20}$ (M = Ti, Ge, Si) nanofibers. The as-prepared BMO nanofibers with diameters of 100–200 nm comprise linked nanoparticles with sizes of about 100 nm. The photocatalytic activities of the resulting $Bi_{12}TiO_{20}$, $Bi_{12}SiO_{20}$ and $Bi_{12}GeO_{20}$ nanofibers for degradation of RhB were evaluated under UV-visible light. Moreover, the electronic structures including the band gap as well as the constitution of the valence bands and conduction bands were discussed.

Experimental

Material synthesis

$Bi(NO_3)_3{\cdot}5H_2O$, tetrabutyl titanate (TBT), tetraethylorthosilicate (TEOS), germanium(IV) ethoxide ($Ge(OEt)_4$), acetic acid (HAc) and *N*,*N*-dimethylformamide (DMF) were of analytical grade, and were supplied by Shanghai Sinopharm Chemical Reagent Co. Ltd., China. Poly(vinylpyrrolidone) (PVP, $M_w \approx 1\,300\,000$) was purchased from Aladdin Chemical Co., Ltd. All the chemicals were used as received without further purification.

The BMO nanofibers were synthesized by a simple electrospinning method. In a typical procedure, the precursor solutions for electrospinning were prepared by dissolving $Bi(NO_3)_3{\cdot}5H_2O$ (2.33 g) and HAc (1 mL) in DMF (20 mL) at room temperature. After stirring for 30 min, TBT, TEOS or $Ge(OEt)_4$ were added slowly into the above solution according to the stoichiometric composition, with the Bi/M molar ratio of 12. After the mixtures were stirred for 1 h at room temperature, 2.5 g of PVP was added. The mixtures were stirred overnight, and three transparent precursor solutions for preparing $Bi_{12}MO_{20}$ (M = Ti, Ge, Si) were obtained. These precursor solutions were delivered into a plastic syringe equipped with a 20-gauge stainless steel needle. The feeding rate was 1 mL h^{-1} monitored by a syringe pump. The metallic needle clamped with an electrode was connected to a variable high-voltage power supply, and a collector of aluminum foil served as the grounded counter electrode 12 cm away from the tip of the needle. As a high voltage of 15 kV was applied, the composite nanofibers were formed. The as-collected electrospun fibers were dried at 80 °C in air for 6 h. Subsequently, the composite fibers were calcined at 600 °C in air for 30 min at a heating rate of 2 °C min^{-1}. For comparison, BMOs crystallites were prepared by a traditional solid-state reaction (SSR) at 600 °C in air for 2 h. These samples are denoted as BTO-SS, BSO-SS and BGO-SS, respectively.

Materials characterization

X-ray diffraction (XRD) analysis was performed using a Rigaku D/MAX-RB diffractometer using filtered Cu Kα radiation. The full diffraction patterns of the products were taken in the 2θ range from 10° to 80° at a step model with a step size of 0.02°. The morphology of the samples was characterized using a field emission scanning electron microscope (FESEM, SIRION200, Holland; accelerating voltage: 10 kV). Transmission electron microscopy (TEM) and high-resolution transmission electron microscopy (HRTEM) images were recorded using a JEOL JEM-2010F microscope. X-ray photoelectron spectroscopy (XPS) measurements were carried out on a VG MultiLab 2000 system with a monochromatic Al Ka X-ray source (ThermoVG Scientific). The thermogravimetric (TG) analysis and differential thermal analysis were performed using a PerkinElmer Diamond TG/DSC apparatus. TG and DSC were carried out simultaneously at a heating rate of 10 °C min^{-1} in a flowing air. The photoluminescence emission spectra of the samples were recorded on a Hitachi F-4500 fluorescence spectrophotometer at room temperature to investigate the recombination of photo-induced charge carriers. UV-vis diffuse reflectance spectra were recorded on a SHIMADZU UV-2550 spectrophotometer with an integrating sphere, and $BaSO_4$ was used as the reference.

Theoretical calculations

All density functional theory (DFT) calculations were performed using the projector augmented wave method[35] as implemented in the Vienna ab initio simulation package (VASP).[36,37] The Perdew–Burke–Ernzerhof (PBE) functional[38] of the generalized gradient approximation (GGA) was used as the exchange–correlation function. To improve the DFT-GGA calculations which usually underestimate the band gaps of semiconductors and insulators, we used the hybrid functional Heyd–Scuseria–Ernzerhof (HSE) method.[39] The exchange correlation functional was taken as the screened HSE06 hybrid functional with a screening parameter of 0.2 $Å^{-1}$ and a portion $\alpha = 25\%$ of exact nonlocal Hartree–Fock exchange was mixed into the exchange part of the PBE functional.[40] According to the XRD patterns, the BMO structures are cubic and they are modeled as Fig. 1, with a lattice constant of 10.013 Å and a total of 66 atoms in a supercell. We considered that the cation of the minor component M is substituted by Si, Ge and Ti, respectively. The geometry optimizations were performed under the electron wave function with expansion in plane wave to a cutoff energy of 400 eV and the Monkhorst–Pack *k*-point mesh of 3 × 3 × 3. The optimal atomic positions are obtained until the magnitude of the Hellmann–Feynman force on each atom is less than 0.05 eV $Å^{-1}$.

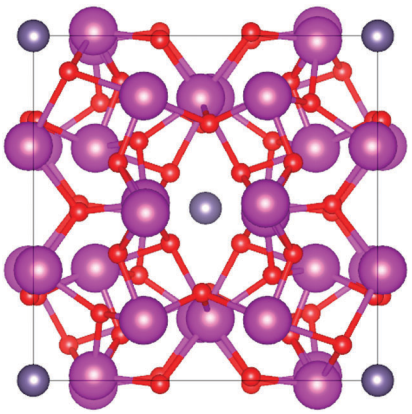

Fig. 1 Supercell model for bulk BMO (66 atoms). The red, purple, and grey spheres represent O, Bi and M (Si, Ge or Ti) atoms, respectively.

Activity evaluation

The photochemical reactor was a self-made cylindrical glass vessel with a water-cooling jacket. Photocatalytic activities of the as-prepared samples were evaluated by monitoring the degradation of RhB as a model organic compound using a 500 W Xe lamp at ambient temperature. The irradiation distance between the lamp and the sample was 12 cm. The photocatalyst (80 mg) was dispersed uniformly into the reactor containing 80 mL of RhB solution (10 ppm). Before irradiation, the suspension was stirred for 30 min and kept in the dark until ensuring an adsorption–desorption equilibrium. At a certain time interval, 3 mL of the reaction solution was taken, centrifuged, and measured on a UV-vis spectrometer at a maximum absorption wavelength of 554 nm.

Results and discussion

The XRD patterns of the products obtained by annealing the as-spun precursor nanofibers at 600 °C in air for 30 min are shown in Fig. 2. The XRD patterns show that all the resulting nanofibers are well crystallized. The diffraction peaks for BTO, BSO, and BGO nanofibers can be readily indexed to cubic $Bi_{12}TiO_{20}$ (JCPDS 34-0097), cubic $Bi_{12}SiO_{20}$ (JCPDS 37-0485), and cubic $Bi_{12}GeO_{20}$ (JCPDS 34-0096), respectively. The corresponding position and intensity of these patterns are similar, since $Bi_{12}TiO_{20}$, $Bi_{12}SiO_{20}$ and $Bi_{12}GeO_{20}$ are isostructural (space group *I*23) and have quasi-identical chemical composition (differing by just one atom in the 33-atom unit cell).[18] It is also confirmed that the organic substances in the BMO precursor nanofibers could be removed by annealing at 600 °C for 30 min as indicated by TG/DSC analysis (Fig. S1, see ESI†). For comparison, we have prepared BTO-SS, BSO-SS, and BGO-SS crystallites by a conventional solid-state reaction. It should be noted that pure cubic $Bi_{12}TiO_{20}$, $Bi_{12}SiO_{20}$, and $Bi_{12}GiO_{20}$ could also be obtained (Fig. S2, see ESI†).

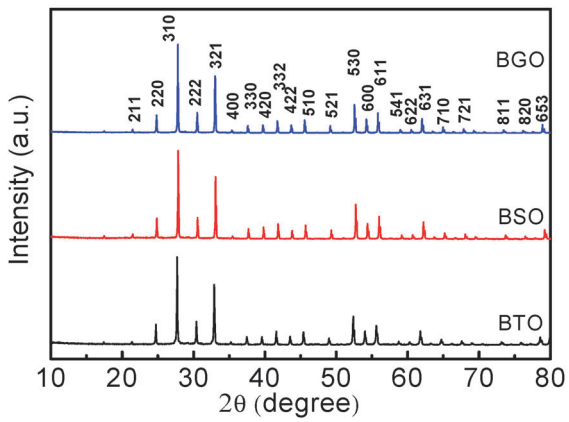

Fig. 2 XRD patterns of the $Bi_{12}MO_{20}$ products obtained by annealing the as-spun precursor nanofibers at 600 °C.

Representative FESEM images of the products are shown in Fig. 3. The as-spun BMO precursor nanofibers with diameters of about 100–300 nm were obtained by electrospinning (Fig. 3a, d and g). Clearly, these nanofibers with smooth surfaces are uniform and have lengths up to several millimeters. After thermally treating the as-spun BMO precursor nanofibers at 600 °C, the morphology of the 1D nanoarchitecture was still retained. However, the surface of the as-prepared BMO nanofibers tends to be rougher. Typically, the BMO nanofibers have diameters of about 100–200 nm, and exhibit a bit of shrinkage compared to their precursors (Fig. 3b, e and h). The EDX microanalysis (Fig. 3c, f and i) indicates the presence of Ti (Si or Ge), Bi and O in these BMO nanofibers. Therefore, the present electrospinning process is a general strategy for preparing sillenite $Bi_{12}MO_{20}$ (M = Ti, Ge, Si) nanofibers. The typical FESEM images of the as-prepared BTO-SS, BSO-SS, and BGO-SS are shown in Fig. S3 (see ESI†). All of them exhibit the particle morphology with sizes of about 1 μm.

To provide further insights into the morphology and structure of the as-prepared BMO nanofibers, TEM investigations were carried out. Fig. 4a, d and g display the representative TEM images of the products, indicating the typical fiber morphology. The as-prepared BMO nanofibers comprise linked nanoparticles with sizes of about 100 nm. Their corresponding selected-area electron diffraction (SAED) patterns are displayed in Fig. 4b, e and h, which indicate that the as-formed BMO nanoparticles are single-crystalline in nature. They can be indexed to the [−111] zone axis of the cubic-structured $Bi_{12}TiO_{20}$, the [001] zone axis of the cubic-structured $Bi_{12}SiO_{20}$, and the [−113] zone axis of the cubic-structured $Bi_{12}GeO_{20}$, respectively. Fig. 4c, f and i show the HRTEM images of the edge of an individual BMO nanofiber. These HRTEM images support the claim of crystallinity for the BMO nanofibers. Furthermore, the HRTEM images of BMO nanofibers are in good accordance with the XRD results (Fig. 2). The periodic fringe spacing of ~2.7 Å corresponds to interplanar spacing between the (321) planes of $Bi_{12}TiO_{12}$, ~2.7 Å for the (321) planes of $Bi_{12}SiO_{12}$, and ~2.7 Å for the (321) planes of $Bi_{12}GeO_{12}$, respectively.

Important information on the surface chemical state and the composition of the final products can be further provided by XPS. The binding energies obtained in the XPS analysis were corrected for specimen charging by referencing the C 1s line to

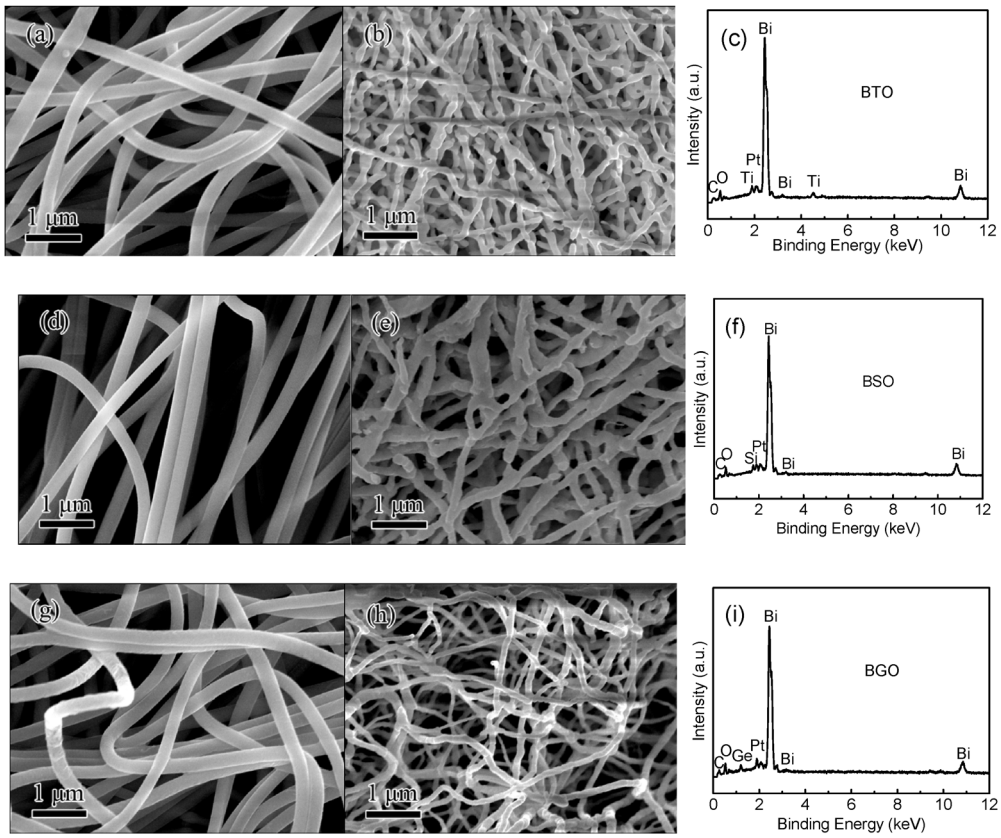

Fig. 3 FESEM images of the as-spun precursor for (a) BTO, (d) BSO, and (g) BGO. The FESEM images of the as-formed sillenite nanofibers are shown in (b) BTO, (e) BSO, and (h) BGO. (c, f, i) EDX spectra of the as-obtained BMO nanofibers. Atomic ratios by EDX: Bi : Ti = 31.75 : 2.21; Bi : Si = 27.87 : 2.37; Bi : Ge = 33.73 : 2.40.

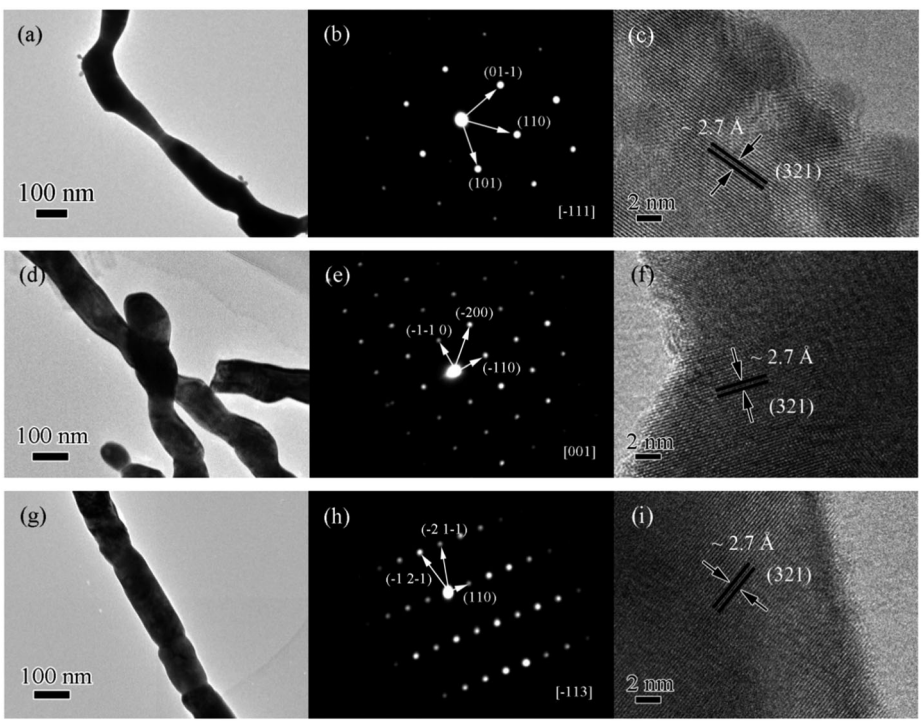

Fig. 4 BTO nanofibers: (a) TEM image, (b) SAED pattern and (c) HRTEM image. BSO nanofibers: (d) TEM image, (e) SAED pattern and (f) HRTEM image. BGO nanofibers: (g) TEM image, (h) SAED pattern and (i) HRTEM image.

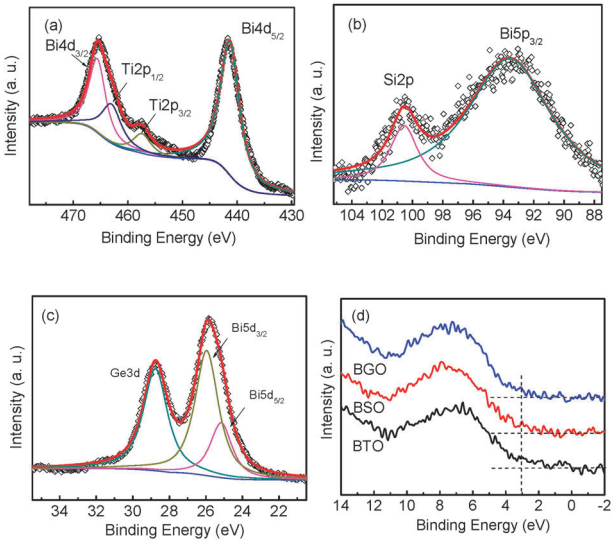

Fig. 5 (a) High-resolution XPS spectra of Bi 4d and Ti 2p of the BTO sample. (b) High-resolution XPS spectra of Bi 5p and Si 2p of the BSO sample. (c) High-resolution XPS spectra of Bi 5d and Ge 3p of the BGO sample. (d) VB XPS spectra of BTO, BSO, and BGO.

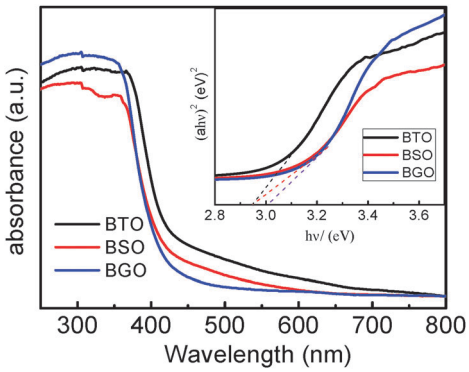

Fig. 6 UV-vis diffuse reflectance spectra of the BMO nanofibers. The inset shows the relationship between $(\alpha h\nu)^2$ and photon energy.

284.5 eV. The survey XPS spectra (Fig. S4, see ESI†) of the as-prepared products reveal that the nanofibers are composed of Bi, Ti, and O for BTO, Bi, Si, and O for BTO, and Bi, Ge, and O for BGO, respectively, which are consistent with the EDX and XRD results. The peaks of Ti $2p_{1/2}$ and Bi $4d_{3/2}$ are partially overlapped (Fig. 5a), leading to a broad bump in the vicinity of 464.5 eV. The XPS peaks at 441.4 and 465.4 eV are assigned to Bi $4d_{5/2}$ and Bi $4d_{3/2}$, respectively. The Ti $2p_{3/2}$ and Ti $2p_{1/2}$ peaks with a typical spin–orbit doublet of 5.7 eV are at 457.3 and 463.0 eV, respectively, which are characteristic of Ti(IV). Similarly, the Si 2p and Ge3d peaks were further examined by high-resolution XPS (Fig. 5b and c). The Si 2p peak is centered at 100.6 eV, and the Ge 3d peak is found at 28.76 eV, which are characteristic of Si(IV) and Ge(IV). In the XPS analysis, not only the information on the binding energy of a specific element but also the total density of states (DOS) of the valence band (VB) can be obtained.[41] Similar diffusive electronic states were observed above the valence band edges of BTO, BSO and BTO nanofibers, as shown in Fig. 5d. It is reasonable that these states are apparently due to the identical contributions of the O 2p orbitals in BTO, BSO and BGO, respectively.[42] A slight difference in the valence band edges of BTO, BSO and BTO could result from the different effects of Bi, Ti, Si, and Ge on the valence band, respectively.

The UV-visible diffuse reflectance spectra in the wavelength range of 300–800 nm for the BMO products are shown in Fig. 6. The three nanofibers have low absorbance in the visible-light range. The relatively long-tail absorption of BTO can be found compared with BSO and BGO in the visible-light region. The absorbance spectra reveal that the difference in the absorption edges appears among the samples, probably arising from the differences in the crystal structures. As the optically active center in the BMOs is Bi, the optical characteristics of the BMOs depend on the nature of the M ions only to some extent, which may affect their geometry, Bi–O distances, and electronic structure.[18] The band-gap values were calculated from the UV-visible absorption spectra according to the following equation:

$$\alpha h\nu = A(h\nu - E_g)^{n/2}$$

where α, $h\nu$, A and E_g signify the absorption coefficient, photo energy, proportionality constant and band gap, respectively. n is equal to 1 or 4, depending on whether the transition is direct or indirect, respectively. BTO was used as an example for judging the character of E_g. The fundamental absorption of BTO involves a direct transition between bands,[11] thus $n = 1$. The energy of the band gap is calculated by extrapolating a straight line to the abscissa. The inset of Fig. 6 shows the plot of the $(\alpha h\nu)^2$ *versus* $h\nu$. The band gaps of the products are estimated to be 2.94 eV for BTO, 2.95 eV for BSO, and 3.05 eV for BGO.

Photoabsorption is a reflection of a material's band structure. Computationally, the band structures and partial densities of states (PDOS) of BMOs were calculated using the hybrid density functional with HSE06 (Fig. 7) for comparison. We note that there is no spin polarization for all the BMOs. The calculated band structures show that the band gaps are 3.28 eV, 3.43 eV, and 3.26 eV for BTO, BSO, and BGO respectively, which are a little larger than the experimental values (2.94 eV for BTO, 2.95 eV for BSO, 3.05 eV for BGO). The narrower band gap of semiconductor photocatalysts not only benefits the absorption of more photons in sunlight, but also promotes the excitation of photogenerated electrons from the valence band (VB) to the conduction band (CB). In the respective band structures of BTO, BSO and BGO, the valence and conduction band extremes locate at the Γ points, indicating that both materials are direct band gap semiconductors. In general, semiconductors with direct band gaps are known to be efficient photocatalysts due to the effective electron–hole excitation.[10] Away from the zone center, coupling with Bi 6s (valence band), Bi 6p (conduction band) and O 2p (valence band) was observed. The interaction between Bi and O atoms may improve the generation and separation of the photoexcited electron–hole pairs and thus enhance the photocatalytic activity of the BMO structures.[5]

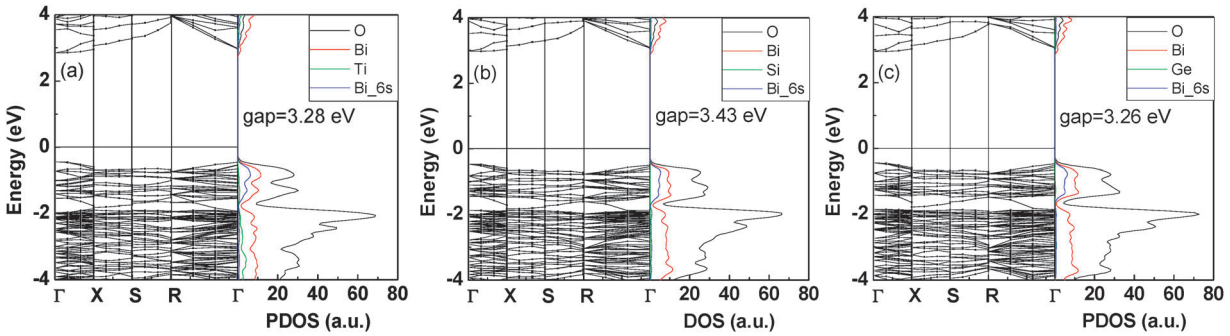

Fig. 7 Band structures and partial density of states of BTO (a), BSO (b) and BGO (c).

To explore the contributions of each atom to the valence bands and conduction bands, the partial and projected density of states (PDOS) of these three BMO structures are shown in the right column of Fig. 7. According to PDOS, we find that the valence band maximum (VBM) is dominated by the O atoms and the conduction band minimum (CBM) is mostly contributed by Bi atoms for these three cases. Additionally, Bi 6s and 6p states also contribute a lot to the VBM. On the other hand, a significant contribution of the Bi 6p states to the CBM can be observed for all three BMOs. It is noticed that the VBM and CBM are mostly determined by the states of Bi and O atoms. The dopant atoms of Si and Ge show no contribution to the band structure in the energy range of several eV near the Fermi level. The case of Ti is quite different, and shows significant contribution of the VB and CB in the same range. According to PDOS, it can be deduced that the generation and separation of the photoexcited electron–hole pairs should take place between Bi and O atoms, and modification of the Bi and O states may be an effective way to enhance the photocatalytic performance of BMOs. From these results, it is concluded that the nature of the M ion contributes to the photocatalytic characteristics of BMOs to some extent, but the optically active center in the BMOs is still the Bi ion.

The photocatalytic activities of the as-prepared samples were evaluated by monitoring the degradation of RhB in water as the model pollutant under a 500 W Xe lamp. Fig. 8 shows the variation in RhB concentration over the photocatalytic degradation reaction under UV-visible light irradiation. Clearly, the exposure of RhB to UV-visible light does not stimulate obvious self-photodegradation that could be negligible in comparison to the photodegradation of the other samples. After the adsorption–desorption equilibrium, the degradation of RhB on BTO, BGO and BSO nanofibers after 120 min of photocatalytic reaction was about 98%, 99% and 81%, respectively, indicating that all the BMO samples exhibit good photocatalytic activities. Therefore, the BMO nanofibers are promising photocatalysts under UV-visible light irradiation. In particular, BGO exhibits the best photocatalytic activity among the three BMO samples, which may be attributed to its relatively wide band gap and blue shift of the band edge, leading to more absorption of UV light in the UV light range. The photodegradation reaction can also be described by the first-order kinetics with respect to the concentration of the organic compound. The time-dependent decomposition of RhB follows the first-order kinetics, $\ln(C_0/C) = kt$, where t is the irradiation time and k is the apparent rate constant. Fig. S5 (ESI†) shows a comparison of the apparent rate constants for the BTO, BSO and BGO samples. The apparent rate constants were 0.0446 min^{-1} for BTO, 0.0153 min^{-1} for BSO, 0.0574 min^{-1} for BGO and determined using the concentration changes of RhB, as measured using the absorbance at 554 nm. The difference in photocatalytic activity may be assigned to the different band gaps and slight differences in the electronic structures, such as different offsets of the valence band tops. In addition, it is worth noting that the BTO, BSO, and BGO nanofibers prepared by electrospinning exhibit enhanced activities compared to the products obtained by the SSR method, as shown in Fig. S6 (see ESI†). The nanofibrous architecture contributes to not only more active sites but also more efficient transfer of the photogenerated charges. Moreover, the smaller particles in the nanofibers contribute to a decrease in the electron–hole recombination because of the reduced diffusion distance of photogenerated charges from the inside of particles to the outside surface, which resulted in the enhancement of photocatalytic activities.[16]

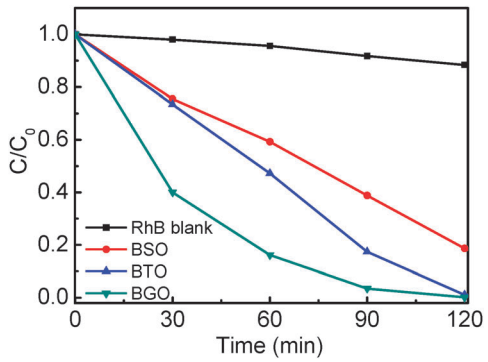

Fig. 8 Degradation profiles of RhB over different samples where C is the concentration of the RhB and C_0 is the initial concentration of the RhB after adsorption–desorption equilibrium.

The photoluminescence emission spectra can be used to evaluate the separation capability of the photo-induced carriers. The higher PL intensity might indicate a higher recombination rate of photo-generated electrons and holes.[43] The room temperature PL emission spectra of the three BMO nanofibers are shown in

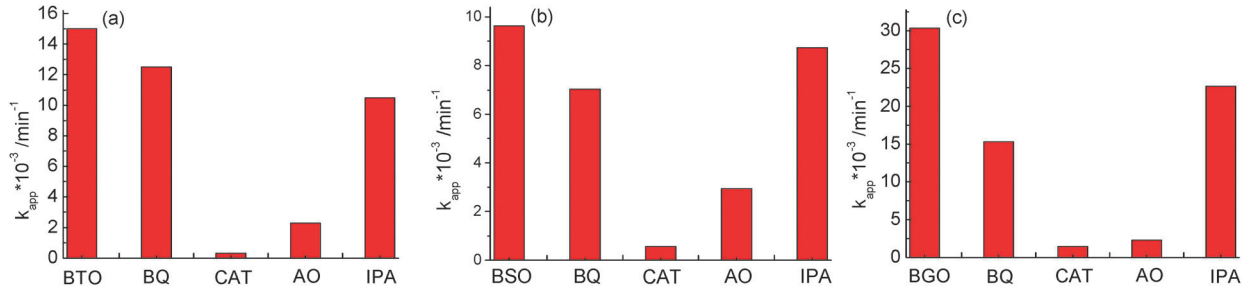

Fig. 9 The effects of different scavengers on the degradation of RhB over (a) BTO, (b) BSO, and (c) BGO.

Fig. S7 (ESI†). The shape and the position of the three curves are nearly the same. When excited by 320 nm, two emission peaks at around 429 and 469 nm are observed for the BTO sample. The emission intensity of the peaks from the BSO and BGO nanofibers changes a little. This suggests that the separation capabilities of photogenerated charge carriers for the three BMO samples are similar during the photocatalytic reactions, which may be related to the similar band structures of the BMOs.

The degradation of organic pollutants by semiconductor-mediated photodegradation is believed to be controlled by free-radical chemistry.[44] In a photocatalytic degradation system, the band–band excitation produces the reductive conduction band electrons (e^-) and oxidative valence band holes (h^+) (eqn (1)). The holes can react with surface adsorbed H_2O to produce $^\bullet OH$ radicals (eqn (2)). The conduction band electrons are usually scavenged by O_2 to yield superoxide radical anions $^\bullet O_2^-$ (eqn (3)). H_2O_2 is a rather oxygen-bearing species and the formation is mainly attributed to the disproportionation or the one electron reduction of $^\bullet O_2^-$ (eqn (4) and (5)).[44] A conventional method to probe the role of reactive species is to add a suitable radical quencher into the systems, by which the contribution of the targeted reactive species is estimated from the effect of the probes on the reaction rate.[44–46]

$$\text{Catalyst} + h\nu \rightarrow e^- + h^+ \quad (1)$$

$$H_2O + h^+ \rightarrow {}^\bullet OH + H^+ \quad (2)$$

$$e^- + O_2 \rightarrow {}^\bullet O_2^- \quad (3)$$

$$2{}^\bullet O_2^- + 2H^+ \rightarrow O_2 + H_2O_2 \quad (4)$$

$$^\bullet O_2^- + e^- + 2H^+ \rightarrow H_2O_2 \quad (5)$$

To investigate the photocatalytic mechanism of BMOs in detail, a series of quenchers were employed to scavenge the counterpart active species. Isopropanol (IPA 0.01 M), benzoquinone (BQ 0.01 M), ammonium oxalate (AO 0.01 M), and catalase (CAT 500 mg L^{-1}) were introduced to the reaction system as the scavenger of $^\bullet OH$, $^\bullet O_2^-$, h^+, and H_2O_2 radical species, respectively.[45–48] The control experiment was also performed without using any quencher under the identical conditions. If the degradation efficiency is greatly reduced, it indicates that the oxidizing species play a more important role in the reaction. As shown in Fig. 9, it can be observed that the degradation of RhB was obviously depressed by the addition of CAT and AO, while the addition of IPA and BQ had a relatively small effect on the degradation of RhB. It means that h^+ and H_2O_2, especially H_2O_2, jointly dominate the photodegradation process of RhB for BTO, BSO, and BGO nanofibers. Besides, the effect of $^\bullet O_2^-$ in the BTO system is nearly negligible while $^\bullet OH$ causes a relatively small impact on degradation of RhB, which is slightly different compared with that in BSO and BGO systems. Based on the above results, it is concluded that BTO, BSO, and BGO may follow a similar photocatalytic mechanism in photodegradation of RhB.

Conclusions

The sillenite $Bi_{12}MO_{20}$ (M = Ti, Ge, Si) nanofibers with diameters of 100–200 nm have been successfully fabricated through an electrospinning method combined with subsequent annealing. The BTO, BSO, and BGO nanofibers are isostructural and have quasi-identical chemical compositions. The band gaps of the $Bi_{12}MO_{20}$ products are estimated to be 2.94 eV for BTO, 2.95 eV for BSO, 3.05 eV for BGO *via* DRS. The as-prepared BTO, BSO, and BGO nanofibers show excellent photocatalytic activity for photodecomposition of RhB under UV-visible light irradiation. A photocatalytic mechanism is proposed that h^+ and H_2O_2, especially H_2O_2, dominate simultaneously the photodegradation process of RhB. The effect of $^\bullet O_2^-$ on the BTO photocatalysis is relatively weak while the effect of $^\bullet OH$ could be hardly detectable, which is slightly different from BSO and BGO. The phenomena could be attributed to the different microstructures, band gaps, and electronic structures such as different valence bands and conduction bands, which depend on the nature of the M ion. Furthermore, this work provides a facile, versatile strategy to prepare $Bi_{12}MO_{20}$ (M = Ti, Ge, Si) nanofibers and this method can be extended to fabricate other functional 1D nanostructures for diverse applications.

Acknowledgements

This work was supported by the Natural Science Foundation of China (Grant Nos. 21271078 and 51002057), PCSIRT (Program for Changjiang Scholars and Innovative Research Team in University), and NCET (Program for New Century Excellent Talents in University, No. NECT-12-0223). The authors thank the Analytical and Testing Center of HUST for XRD, SEM, and TEM measurements.

Notes and references

1 X. Wang, K. Maeda, A. Thomas, K. Takanabe, G. Xin, J. M. Carlsson, K. Domen and M. Antonietti, *Nat. Mater.*, 2009, **8**, 76–80.
2 X. Chen, X. Wang and X. Fu, *Energy Environ. Sci.*, 2009, **2**, 872–877.
3 K. Ariga, S. Ishihara, H. Abe, M. Li and J. P. Hill, *J. Mater. Chem.*, 2012, **22**, 2369–2377.
4 X. Chen, S. Shen, L. Guo and S. S. Mao, *Chem. Rev.*, 2010, **110**, 6503–6570.
5 M. Shang, W. Z. Wang, L. Zhang, S. M. Sun, L. Wang and L. Zhou, *J. Phys. Chem. C*, 2009, **113**, 14727–14731.
6 X. Hu, G. Li and J. C. Yu, *Langmuir*, 2009, **26**, 3031–3039.
7 C. Li, F. Wang and J. C. Yu, *Energy Environ. Sci.*, 2011, **4**, 100–113.
8 D. Zhang, G. Li and J. C. Yu, *J. Mater. Chem.*, 2010, **20**, 4529–4536.
9 G. Dai, J. Yu and G. Liu, *J. Phys. Chem. C*, 2011, **115**, 7339–7346.
10 H. Liu, J. Yuan, Z. Jiang, W. Shangguan, H. Einaga and Y. J. Teraoka, *J. Mater. Chem.*, 2011, **21**, 16535–16543.
11 W. Wei, Y. Dai and B. Huang, *J. Phys. Chem. C*, 2009, **113**, 5658–5663.
12 H. Zhang, P. Wu, Y. Li, L. Liao, Z. Fang and X. Zhong, *ChemCatChem*, 2010, **2**, 1115–1121.
13 J. Jiang, K. Zhao, X. Xiao and L. Zhang, *J. Am. Chem. Soc.*, 2012, **134**, 4473–4476.
14 W. J. Jo, J. W. Jang, K. J. Kong, H. J. Kang, J. Y. Kim, H. Jun, K. P. Parmar and J. S. Lee, *Angew. Chem., Int. Ed.*, 2012, **51**, 3147–3151.
15 L. Zhou, M. Yu, J. Yang, Y. Wang and C. Yu, *J. Phys. Chem. C*, 2010, **114**, 18812–18818.
16 D. Hou, W. Luo, Y. Huang, J. C. Yu and X. Hu, *Nanoscale*, 2013, **5**, 2028–2035.
17 J. Tang, Z. Zou and J. Ye, *Angew. Chem., Int. Ed.*, 2004, **43**, 4463–4466.
18 A. F. Lima, S. A. S. Farias and M. V. Lalic, *J. Appl. Phys.*, 2011, **110**, 083705.
19 J. S. McCullough, A. L. Harmon Bauer, C. A. Hunt and J. J. Martin, *J. Appl. Phys.*, 2001, **90**, 6017–6021.
20 A. W. Wood, C. A. Hunt and J. J. Martin, *J. Appl. Phys.*, 2007, **101**, 063517.
21 I. Ahmad, V. Marinova and E. Goovaerts, *Phys. Rev. B: Condens. Matter Mater. Phys.*, 2009, **79**, 033107.
22 Y. Hu and D. C. Sinclair, *Chem. Mater.*, 2013, **25**, 48–54.
23 V. Marinova, M. Veleva and D. Petrova, *Opt. Mater.*, 2003, **24**, 595–600.
24 W. Yao, H. Wang, X. Xu, X. Cheng, J. Huang, S. Shang, X. Yang and M. Wang, *Appl. Catal., A*, 2003, **243**, 185–190.
25 W. Yao, H. Wang, X. Xu, Y. Zhang, X. Cheng, X. Yang, S. Shang, Y. Liu, J. Zhou and M. Wang, *J. Mol. Catal. A: Chem.*, 2003, **202**, 305–311.
26 X. Zhu, J. Zhang and F. Chen, *Appl. Catal., B*, 2011, **102**, 316–322.
27 J. Hou, R. Cao, S. Jiao, H. Zhu and R. V. Kumar, *Appl. Catal., B*, 2011, **104**, 399–406.
28 C. He and M. Gu, *Scr. Mater.*, 2006, **55**, 481–484.
29 C. He and M. Gu, *Scr. Mater.*, 2006, **54**, 1221–1225.
30 Y. Z. Long, M. Yu, B. Sun, C. Z. Gu and Z. Fan, *Chem. Soc. Rev.*, 2012, **41**, 4560–4580.
31 M. Shang, W. Z. Wang, W. Z. Yin, J. Ren, S. M. Sun and L. Zhang, *Chem.–Eur. J.*, 2010, **16**, 11412–11419.
32 B. Lu, C. Zhu, Z. Zhang, W. Lan and E. Xie, *J. Mater. Chem.*, 2012, **22**, 1375–1379.
33 S. Zhang, Z. Lin, L. Ji, Y. Li, G. Xu, L. Xue, S. Li, Y. Lu, O. Toprakci and X. Zhang, *J. Mater. Chem.*, 2012, **22**, 14661–14666.
34 D. Hou, X. Hu, P. Hu, W. Zhang, M. Zhang and Y. Huang, *Nanoscale*, 2013, **5**, 9764–9772.
35 G. Kresse and D. Joubert, *Phys. Rev. B: Condens. Matter Mater. Phys.*, 1999, **59**, 1758–1774.
36 G. Kresse and J. Furthmuller, *Comput. Mater. Sci.*, 1996, **6**, 15–50.
37 G. Kresse and J. Furthmuller, *Phys. Rev. B: Condens. Matter Mater. Phys.*, 1996, **54**, 11169–11185.
38 J. P. Perdew, K. Burke and M. Ernzerhof, *Phys. Rev. Lett.*, 1996, **77**, 3865–3868.
39 J. Heyd, G. E. Scuseria and M. Ernzerhof, *J. Chem. Phys.*, 2003, **118**, 8207–8215.
40 A. V. Krukau, O. A. Vydrov, A. F. Izmaylov and G. E. Scuseria, *J. Chem. Phys.*, 2006, **125**, 224106.
41 X. Chen and C. Burda, *J. Am. Chem. Soc.*, 2008, **130**, 5018–5019.
42 X. Chen, P.-A. Glans, X. Qiu, S. Dayal, W. D. Jennings, K. E. Smith, C. Burda and J. Guo, *J. Electron Spectrosc. Relat. Phenom.*, 2008, **162**, 67–73.
43 H. Liu, W. Cao, Y. Su, Y. Wang and X. Wang, *Appl. Catal., B*, 2012, **111–112**, 271–279.
44 C. Chen, W. Ma and J. Zhao, *Chem. Soc. Rev.*, 2010, **39**, 4206–4219.
45 G. Li, K. H. Wong, X. Zhang, C. Hu, J. C. Yu, R. C. Chan and P. K. Wong, *Chemosphere*, 2009, **76**, 1185–1191.
46 J. Cao, B. Xu, H. Lin, B. Luo and S. Chen, *Chem. Eng. J.*, 2012, **185–186**, 91–99.
47 M. Yin, Z. Li, J. Kou and Z. Zou, *Environ. Sci. Technol.*, 2009, **43**, 8361–8366.
48 J. Cao, B. Xu, B. Luo, H. Lin and S. Chen, *Catal. Commun.*, 2011, **13**, 63–68.